COMSOL CONFERENCE 2026 CAMBRIDGE

Simulation-Driven Design of Point-Heating Seebeck Cells: Electrode Material Optimization for ZnO Thin Films

Hadiqa Naaz[1*], Saeid Izadshenas Jahromi[1], José Ordonez-Miranda[2], Andreas D. Wieck[3], Michał Pawlak[1],

1. Institute of Physics, Faculty of Physics, Astronomy and Informatics, Nicolaus Copernicus University, Grudziądzka 5, 87-100 Toruń, Poland.
2. Sorbonne Université, CNRS, Institut des NanoSciences de Paris (INSP), Paris, France.
3. Faculty of Physics & Astronomy, Ruhr University Bochum, Bochum, Germany.
Corresponding author: Hadiqa@doktorant.umk.pl

Abstract

Thermoelectric Seebeck cells convert waste heat directly into electrical energy, but their practical deployment is limited by electrode material selection and by heat spreading that degrades the thermal gradient (ΔT) driving the measurement. To address this challenge, a coupled thermal–electrical finite-element model was developed in COMSOL Multiphysics® to simulate a localized point-heating Seebeck measurement cell for a 5 × 5 mm^2 ZnO thin film with a thickness of 500nm, using Platinum (Pt) and Copper (Cu) as comparative point-contact electrodes. The Heat Transfer in Solids and Electric Currents interfaces were self-consistently coupled through a Thermoelectric Effect node to resolve the three-dimensional temperature and electric potential fields under an applied inward heat flux and grounded cold-end boundary condition. Results showed that electrode thermal conductivity strongly governs axial thermal confinement: the lower-conductivity Pt electrode sustained a markedly steeper temperature gradient and higher interfacial temperature (85 °C) than Cu (70 °C), translating directly into a larger thermoelectric voltage across the ZnO film (22.2 mV for Pt versus 7.8 mV for Cu). Despite this near three-fold difference in absolute voltage response, linear regression of the simulated voltage–temperature data yielded closely matching Seebeck coefficients of −322.95 μV/K and −312.47 μV/K for the Pt and Cu configurations, respectively, both negative in sign and consistent with n-type ZnO conduction, confirming that the extracted Seebeck coefficient is an intrinsic, electrode-independent material property. These findings establish electrode material as a key design parameter for optimizing the sensitivity of Seebeck measurements and validate the simulation framework as a predictive tool for guiding experimental cell design and the development of future bent-electrode geometries.

Keywords: Seebeck effect; thermoelectric sensing; finite element analysis; COMSOL Multiphysics; ZnO thin film; localized point heating.

Introduction

Harvesting waste heat and converting it into electrical energy using thermo-electrochemical cells is an essential strategy for the development of renewable energy [1]. Thermoelectric conversion is based on the Seebeck effect, in which a temperature difference across a material generates an electrical voltage. The Seebeck coefficient is determined from the voltage generated across a sample under an applied temperature difference and, for a temperature-independent (S), is expressed as

$$S = -\frac{\Delta V}{\Delta T} \qquad (1)$$

where (ΔV) is the thermoelectric voltage and (ΔT) is the temperature difference across the sample. Reliable determination of (S) therefore requires accurate control and measurement of the temperature gradient at the sensing region. Various two- and four-point measurement configurations have been developed to improve the accuracy of Seebeck measurements, particularly by reducing the influence of electrical contact resistance and improving temperature determination [2,3].

For thin-film thermoelectric materials, establishing a well-defined temperature gradient is particularly challenging because heat can spread through the electrodes, substrate, and surrounding components, significantly modifying the local temperature distribution. The thermal properties and geometry of the measurement electrodes therefore influence the temperature difference across the active layer and, consequently, the measured Seebeck coefficient [4,5]. Numerical modeling provides an effective approach for resolving these coupled thermal and electrical effects. Finite-element simulations have been used to analyze Seebeck measurement configurations and temperature distributions, including models implemented in COMSOL Multiphysics [6,7].

Theory and Governing Equations

The coupled thermal–electrical response of the point-heated Seebeck cell was modeled using the Heat Transfer in Solids, Electric Currents, and Thermoelectric Effect interfaces in COMSOL Multiphysics®. Thermal transport is governed by

$$\rho C_p \frac{\partial T}{\partial t} + \nabla \cdot (-k\nabla T) = Q \qquad (2)$$

where ρ, C_p, T, Q, and k are the density, specific heat capacity, temperature, volumetric heat source, and thermal conductivity, respectively. The conductive flux is given by Fourier's law,

$$q = -k\nabla T \qquad (3)$$

Where, q is the conductive heat flux (W/m²), $k$is the thermal conductivity (W/m·K), and ∇T is the temperature gradient (K/m).

The point-heater boundary condition is expressed as

$$-n \cdot q = q_{in} \quad (4)$$

Where, q_{in} is the applied heat flux at the point-heater boundary (W/m²).

Electrical charge conservation requires

$$\nabla \cdot J = 0 \quad (5)$$

Where, J is the electric current density (A/m²).

with the thermoelectrically coupled current density given by

$$J = -\sigma \nabla \phi - \sigma S \nabla T \quad (6)$$

where σ, ϕ, and S are the electrical conductivity, electric potential, and Seebeck coefficient, respectively. The second term in Equation (6) directly couples the temperature and electric fields, capturing the thermoelectric contribution to current flow. The open-circuit thermoelectric voltage generated in response to an applied temperature difference is given by

$$\Delta V = -S \Delta T \quad (7)$$

from which the Seebeck coefficient is extracted as

$$S = -\frac{\Delta V}{\Delta T} \quad (8)$$

All simulations were performed under steady-state conditions ($\partial T / \partial t = 0$), such that Equations (2)–(8) were solved self-consistently to obtain the three-dimensional temperature and electric potential fields, from which SS was extracted and compared for the Cu and Pt electrode configurations.

3. Numerical Model

3.1 Electrode Material Comparison Model

A simplified geometry consisting of a hollow alumina (Al_2O_3) cylinder (outer diameter 0.5 mm, length 10 mm) housing a coaxial metallic rod electrode (radius 0.4 mm, length 30 mm) was built in COMSOL Multiphysics® as shown in Figure 1(a). The inner wall of the alumina was in direct thermal contact with the electrode surface. A uniform inward heat flux ($q_0 = 2200$ W/m^2) was applied to the outer surface of the alumina. Axial temperature was probed along the electrode centerline at $x = 15$ mm. Pt and Cu electrodes were compared under identical geometry and boundary conditions to isolate the effect of thermal conductivity on axial heat retention.

3.2 Localized Point-Heating (LPH) Seebeck Cell Model

The complete Seebeck cell (Figures 1–2) consists of a 30 mm wire probe running from a cold-end block, through an alumina heater sleeve, to a mid-edge contact on a 5 x 5 mm² ZnO thin film on a glass substrate. The *Heat Transfer in Solids* and *Electric Currents* interfaces were coupled via a *Thermoelectric Effect* node to solve Eqs. (2)–(8) self-consistently and extract the Seebeck coefficient from the simulated V–ΔT response. An inward heat flux ($q_{\text{in}} = 13000$ W/m^2) was applied at the alumina heater through localized point heating (LPH) at a single point contact, electrical ground ($\phi = 0$) was set at the cold end of the ZnO, and a fixed lower temperature was prescribed at the exposed cold end. A terminal was applied at the hotter end of the ZnO to extract the developed thermoelectric voltage. Pt and Cu point electrodes were compared under identical geometry and boundary conditions to evaluate how the electrode material governs thermal localization and the determination of the Seebeck coefficient under LPH.

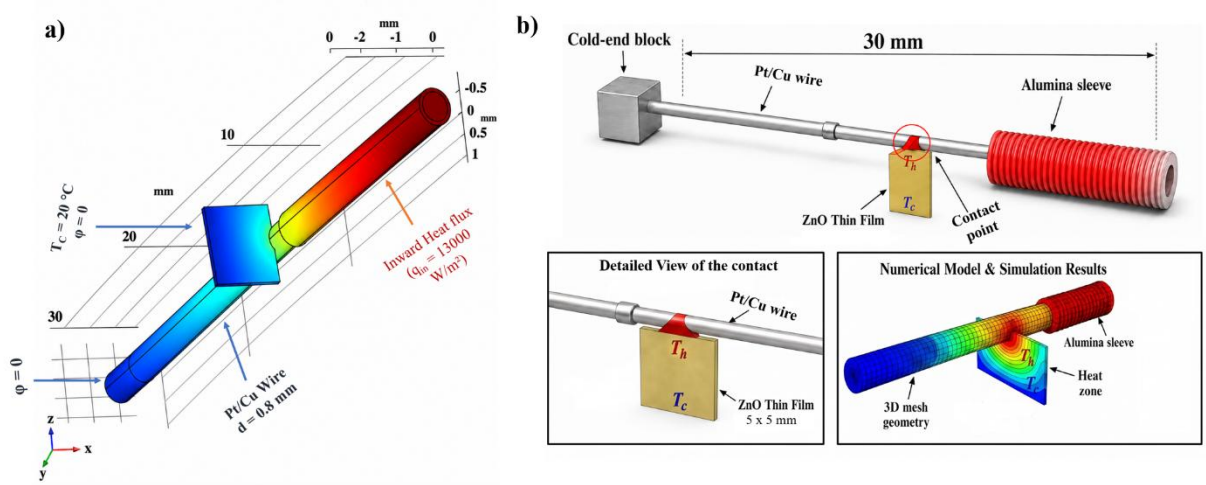


Figure 1. *(a) Geometry and boundary conditions of the point-contact on ZnO thin film in the Seebeck cell, showing the applied heat flux, electrical ground, and external temperature. (b) Schematic of the 30 mm Pt-wire probe contacting the 5 × 5 mm² ZnO thin film, with a detailed view of the contact region and 3D mesh.*

The mesh was locally refined at the contact junction and along the alumina–electrode interface to resolve steep local gradients and geometric singularities introduced by the point contact (Figure 1(b)). Because the electrical conductivity contrast between the alumina insulator and the Pt/Cu electrodes spans approximately eighteen orders of magnitude, the resulting linear systems are numerically stiff. Table 1 summarizes the thermal, electrical, and Seebeck properties of Al_2O_3, Cu, Pt, and ZnO used as inputs for the simulations. Robust convergence was therefore achieved using a direct MUMPS solver in conjunction with a fully coupled Newton nonlinear solver, rather than the default segregated/iterative solution approach.

Table 1. Input properties of the materials used in simulations

Materials	Seebeck Coefficient S (V/K)	Thermal Conductivity k (W/(m·K))	Electrical Conductivity σ (S/m)	Density ρ (kg/m³)	Specific Heat Capacity Cp (J/(kg·K))
Al_2O_3	3.5×10^{-6}	27	1×10^{-12}	3900	900 [8]
Cu	6.5×10^{-6}	400	5.998×10^{7}	8960	385 [9]
Pt	-5×10^{-6}	71.6	8.9×10^{6}	21450	133 [10]
ZnO	-4×10^{-4}	40	1	5610	500 [11], [12]

Simulation Results and Discussion

Effect of Electrode Material on Thermal Localization

To investigate the effect of heat flux on the temperature distribution in the Pt and Cu electrodes, an inward heat flux of $q_{\text{in}} = 2200\ \text{W/m}^2$ was applied at the alumina heater. The cold end was electrically grounded, and the external temperature was maintained at $T_{\text{ext}} = 20\,^{\circ}\text{C}$. Under these conditions, electrode thermal conductivity was found to strongly govern the spatial extent of the induced temperature field. Figure 2 shows the simulated three-dimensional temperature distribution in the Pt and Cu electrodes under identical boundary conditions, while Figure 3 plots the corresponding axial temperature profile along each electrode, with the point-probe location (x = 15 mm) marked.

As shown in Figure 2, the Pt electrode sustains a markedly wider axial temperature span (50–100 °C) than the Cu electrode (5–75 °C), with simulated probe temperatures of 85.052 °C and 69.878 °C, respectively (Figure 3).

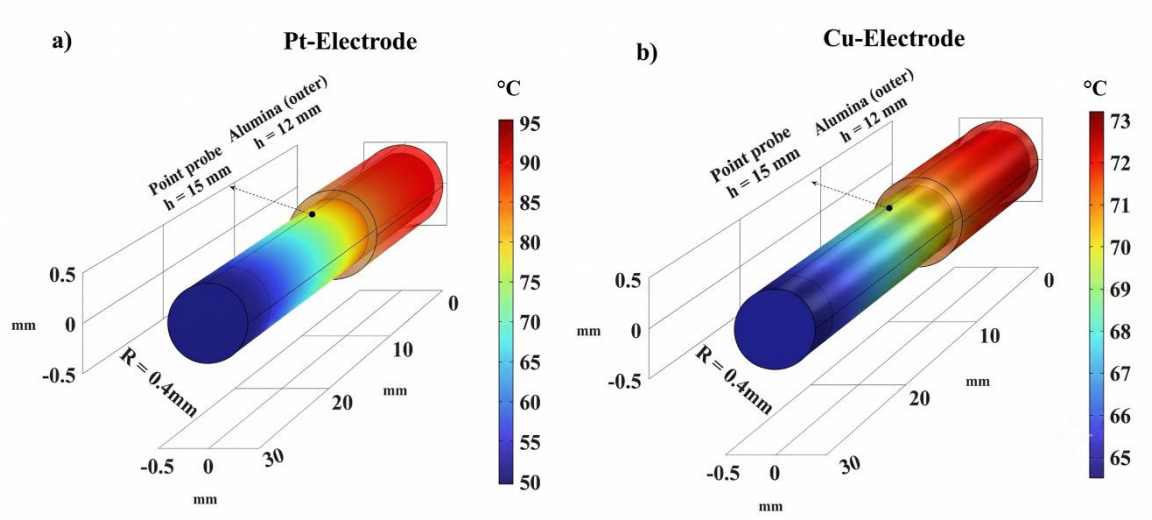


Figure 2. *Simulated 3D temperature distribution in (a) the Pt electrode and (b) the Cu electrode under identical boundary conditions, with point-probe diagnostics at x = 15 mm.*

This trend follows from the steady-state axial conduction equation, whose solution decays with a characteristic length $L_c = \sqrt{kA/hP}$. Since Pt's thermal conductivity (71.6 W/(m·K)) is an order of magnitude lower than Cu's (400 W/(m·K)), its shorter decay length confines heat near the contact zone rather than allowing it to diffuse along the rod, corresponding to a higher axial thermal resistance $R_{th} = L/(kA)$ [13]. Cu's higher conductivity instead produces rapid heat spreading and the flatter, near-isothermal profile seen in Figure 4, consistent with a smaller local Biot number $Bi = hL_c/k$ at the contact interface.

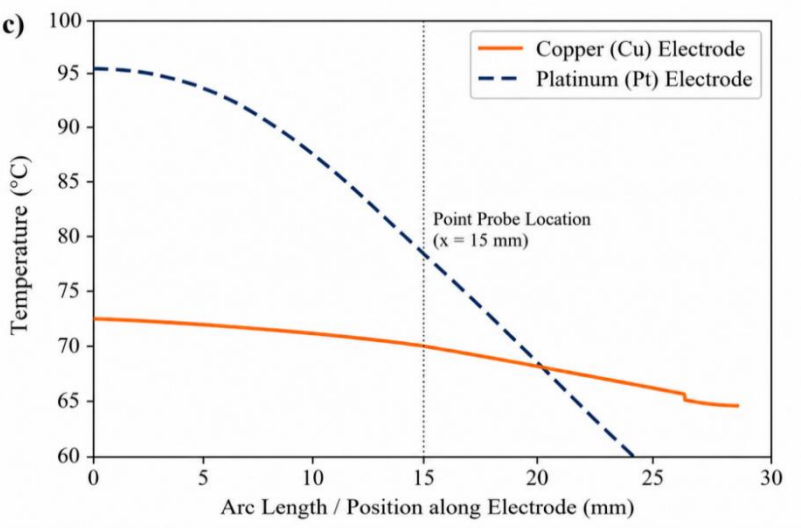


Figure 3. *Temperature distribution along the electrode arc length for Pt and Cu electrodes, illustrating the distinct thermal responses of the two electrode materials. The temperature at the point-probe location (x = 15 mm) is also indicated.*

These results show that electrode selection governs the spatial confinement of the thermal field, not just the peak interface temperature. A lower-conductivity electrode, such as Pt, yields a shorter thermal penetration depth and a larger localized ΔT across the contact interface, both of which are key requirements for high-sensitivity Seebeck measurement.

Temperature and Voltage Distribution in ZnO under Cu and Pt Electrodes

Simulation results revealed a pronounced dependence of the ZnO film temperature and voltage profile on the electrode material employed for heat delivery. For the Pt electrode configuration, the film temperature increased from 20 °C at the grounded end to approximately 83 °C at the heated boundary, whereas the Cu electrode configuration yielded a substantially lower terminal temperature of approximately 42 °C under identical boundary conditions, as evident in Figure 4. In both cases, the temperature profile exhibited near-linear behavior over the initial 4 mm of arc length, consistent with one-dimensional conductive heat transfer along the film. Beyond this region, however, the profile deviated from linearity and exhibited a reduced slope near the heated edge, a signature indicative of two- and three-dimensional heat-spreading effects not accounted for by the simplified 1D conduction assumption. The nearly two-fold difference in terminal film temperature between the Pt and Cu cases was attributed to the disparity in electrode thermal conductivity: the comparatively low thermal conductivity of Pt (71.6 W/(m·K)) limited axial heat dissipation within the electrode, resulting in greater thermal energy transfer into the adjacent ZnO film, whereas the high thermal conductivity of Cu (400 W/(m·K)) facilitated rapid axial heat redistribution, thereby reducing the effective thermal flux delivered to the film. These results demonstrated that electrode material selection governs not only the internal temperature distribution of the electrode but also the magnitude of thermal loading imposed on the ZnO film, a consideration of direct relevance to device designs requiring controlled thermal management of the active layer [14].

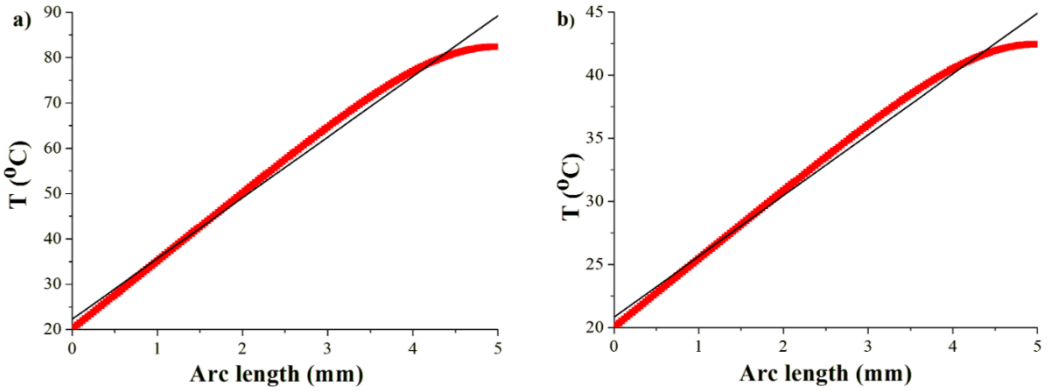


Figure 4. *Simulated temperature distribution (red) along the arc length of the ZnO thin film (5 × 5 mm) heated by the (a) Pt and (b) Cu electrodes, with the corresponding linear fit (black line) shown for comparison.*

The electric potential generated across the ZnO thin film exhibited a strong dependence on the electrode material, as shown in Figure 5. The Pt electrode produced a maximum potential of 22.22 × 10^{-3} V,

nearly threefold higher than the 7.79 × 10^{-3} V generated by the Cu electrode. This disparity was attributed primarily to the Seebeck effect, whereby the temperature gradient established across the ZnO film by each electrode induced a thermoelectric voltage proportional to the local temperature difference, given by $\Delta V = S \cdot \Delta T$, where S is the Seebeck coefficient of ZnO. Since the Pt electrode experienced a larger temperature differential across the film (Figure 4), it correspondingly generated a greater thermoelectric potential, whereas the smaller thermal gradient produced by the Cu electrode yielded a proportionally lower output voltage. This behavior confirmed that the observed potential was not solely due to Ohmic conduction but was predominantly governed by thermally induced charge-carrier diffusion within the semiconducting ZnO film.

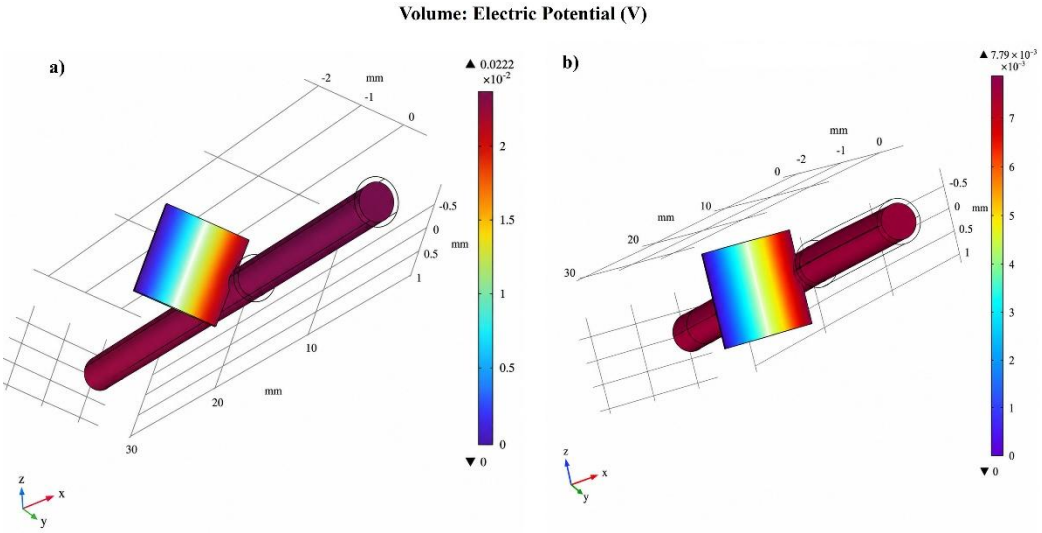


Figure 5. *Simulated three-dimensional electric potential distribution across the ZnO thin film for (a) Pt and (b) Cu electrode configurations, showing maximum potentials of 0.0222 V and 7.79 × 10^{-3} V, respectively, arising from the thermoelectric (Seebeck) response to the imposed temperature gradient.*

The spatial evolution of this thermoelectric potential along the film is presented in Figure 6. The potential increased linearly with arc length in both electrode cases, consistent with a constant Seebeck coefficient and a linear temperature gradient across the film, in accordance with the steady-state thermoelectric relation $V(x) = S \cdot [T(x) - T_0]$. The absence of curvature in the potential profile, despite the mild nonlinearity observed in the corresponding temperature distribution near the contact edge (Figure 4), suggested that the bulk of the film obeyed a linear thermoelectric response, with deviations confined to a narrow region near the heated boundary. The consistently higher potential slope obtained with the Pt electrode further reinforced that the magnitude of the thermoelectric voltage in ZnO was directly governed by the steepness of the imposed temperature gradient rather than by the electrode's electrical conductivity alone.

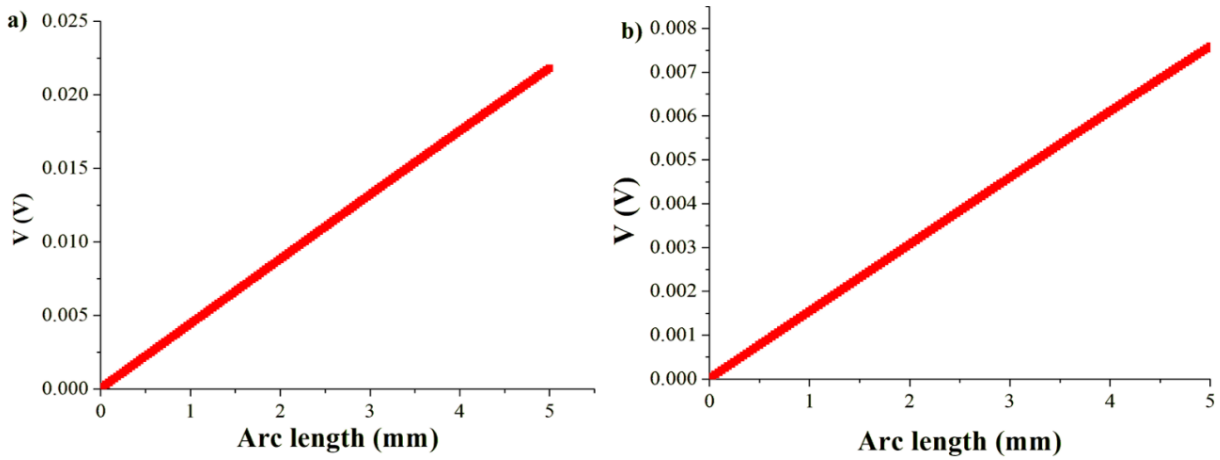


Figure 6. *Electric potential as a function of arc length across the ZnO thin film for the (a) Pt and (b) Cu electrode configurations, showing a linear potential rise from the cold (grounded) end to the hot end, consistent with a Seebeck-driven thermoelectric response in n-type ZnO.*

Seebeck Coefficient Calculation

The Seebeck coefficient of the ZnO thin film was extracted by plotting the simulated thermoelectric potential as a function of the local temperature for both the Pt and Cu electrode configurations, as shown in Figure 7. A linear regression fit to the V–T data yielded Seebeck coefficients of −322.95 μV/K and −312.47 μV/K for the Pt and Cu cases, respectively. While conventional experimental setups relying on global, macro-scale heating stages typically report suppressed Seebeck values (ranging between −150 and −250 μV/K) due to severe substrate heat sinking and thermal parasitics, the localized point-contact configuration successfully circumvents these boundary losses, thereby revealing the material's true intrinsic response [15, 16]. The close agreement between the two extracted values, despite the substantially different absolute temperature ranges spanned in each case, confirmed that the Seebeck coefficient represented an intrinsic property of ZnO, independent of the electrode material or the magnitude of the applied thermal gradient. The negative sign obtained in both cases was consistent with n-type semiconducting behavior, wherein electrons act as the dominant charge carriers and diffuse preferentially from the hot to the cold junction, establishing a potential polarity opposite to that expected for p-type conduction; this result was in agreement with the polarity trend discussed in relation to Figure 6. The V–T curves exhibited predominantly linear behavior over most of the temperature range, consistent with the classical Seebeck relation $V = S \cdot \Delta T$ assuming a temperature-independent Seebeck coefficient. A slight upward curvature was observed at the higher end of the temperature range in both cases, coinciding with the region near the electrode contact where the corresponding temperature profiles (Figure 5) had similarly deviated from linearity due to localized heat spreading; this indicated that the mild nonlinearity in the thermovoltage response originated from the underlying thermal field rather than from an intrinsic temperature dependence of the Seebeck coefficient itself. Overall, the close correspondence between the Seebeck coefficients obtained from the two independent electrode configurations validated the reliability of the simulation framework in capturing the intrinsic thermoelectric response of the ZnO thin film, free from macroscopic thermal dissipation.

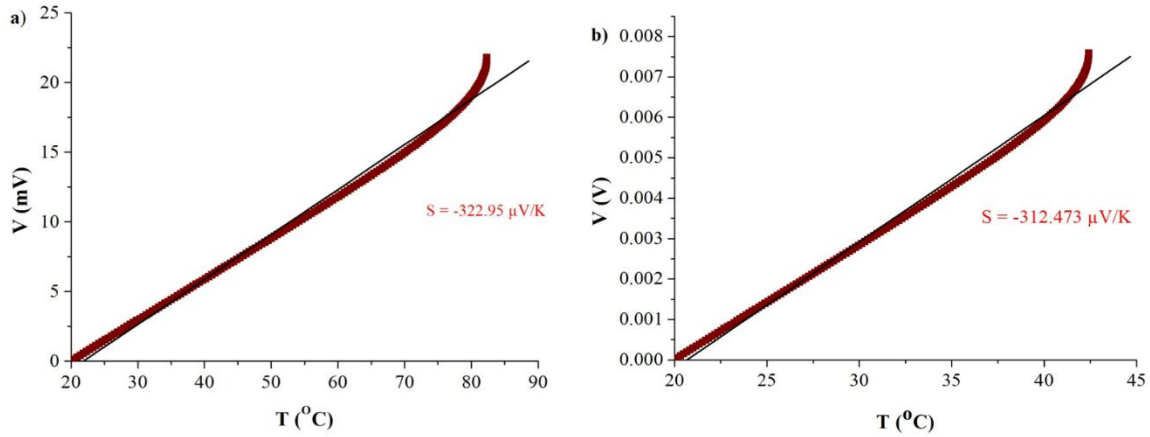


Figure 7. *Simulated thermoelectric potential as a function of local temperature across the ZnO thin film for (a) Pt and (b) Cu electrode configurations, with linear fits (black lines) yielding Seebeck coefficients of −322.95 µV/K and −312.47 µV/K, respectively.*

Conclusions

This study presented a coupled thermal–electrical finite-element framework for evaluating point-contact Seebeck measurements on ZnO thin films, with emphasis on the influence of electrode material on thermal localization and thermoelectric response. Simulations demonstrated that electrode thermal conductivity, rather than the applied heat flux alone, governed the spatial confinement of the temperature field, with the lower-conductivity Pt electrode producing a steeper axial gradient and a greater localized ΔT than the Cu electrode, which in turn yielded a correspondingly larger thermoelectric voltage across the ZnO film. Despite this nearly three-fold difference in absolute voltage output, the extracted Seebeck coefficients converged to closely matching values (−322.95 µV/K and −312.47 µV/K for Pt and Cu, respectively), consistent in sign and magnitude with n-type ZnO, thereby confirming the intrinsic, electrode-independent nature of the Seebeck coefficient and validating the reliability of the simulation framework. Future work will extend this model to bent and curved electrode geometries to evaluate their effect on local heat flux distribution and interfacial ΔT, offering a route to further enhance thermal confinement beyond straight-wire configurations. The geometric and material parameters identified as optimal in this study will subsequently guide the design and fabrication of a physical point-contact Seebeck measurement cell in the experimental laboratory, with experimental validation against the simulated V–T response expected to establish a reliable, simulation-informed platform for characterizing thermoelectric thin films such as ZnO.

References

[1] T. Miao, W. Ma, X. Zhang, and Z. Li, "A self-heating 2ω method for Seebeck coefficient measurement of thermoelectric materials," *Review of Scientific Instruments*, vol. 82, no. 2, p. 024901, 2011.

[2] Q. Fu, Y. Xiong, W. Zhang, and D. Xu, "A setup for measuring the Seebeck coefficient and the electrical resistivity of bulk thermoelectric materials," *Review of Scientific Instruments*, vol. 88, no. 9, p. 095111, 2017.

[3] J. Corcoran, S. Raja, and P. B. Nagy, "Improved thermoelectric power measurements using a four-point technique," *NDT & E International*, vol. 94, pp. 92–100, 2018.

[4] J.-H. Bahk, T. Favaloro, and A. Shakouri, "Thin film thermoelectric characterization techniques," *Annual Review of Heat Transfer*, vol. 16, no. 1, pp. 51–99, 2013.

[5] G. G. Dalkiranis, J. H. C. Bocchi, B. B. M. Torres, A. F. Lopeandia, O. N. Oliveira, and G. C. Faria, "Measurement system to determine the Seebeck coefficient and electrical conductivity of thin films," *IEEE Transactions on Instrumentation and Measurement*, vol. 74, pp. 1–6, 2025.

[6] S. Biswas, A. S. Dutt, N. Sebastian, and V. B. Kamble, "Simple, reversible gradient Seebeck coefficient measurement system for 300–600 K with COMSOL simulations," *Review of Scientific Instruments*, vol. 92, no. 4, p. 044903, 2021.

[7] G. Wang et al., "A thermo-electrochemical cell with a threaded graphite electrode towards low-grade heat recovery," *Journal of Materials Chemistry A*, vol. 13, pp. 2105–2114, 2025.

[8] Y. Kim, J. Lee, and D. S. Kim, "Fabrication of Al2O3/ZnO and Al_2O_3/Cu Reinforced Silicone Rubber Composite Pads for Thermal Interface Materials," *Polymers*, vol. 13, no. 19, p. 3259, 2021.

[9] M. L. G. Moreno, A. B. C. Silva, and R. Dunin-Borkowski, "Dynamics of a Cu/ZnO/Al_2O_3 catalyst revealed by operando transmission electron microscopy during CO2 hydrogenation," *Nature Catalysis*, vol. 9, pp. 312–321, 2026.

[10] L. Zhou, B. Xu, and B. Hou, "Resistivity, Seebeck coefficient, and thermal conductivity of solid fcc Pt from first principles," *Physical Review B*, vol. 100, no. 21, p. 214302, 2019.

[11] V. Fitriyani, T. B. Prayitno, and I. Sugihartono, "Thermoelectric Properties of ZnO Wurtzite Structure by Density Functional Theory," *Journal of Physics: Conference Series*, vol. 3034, p. 012010, 2025.

[12] S. Choi, J. H. Park, and M. W. Oh, "Charge transport and thermoelectric properties of ZnO-carbon nanomaterials composites," *KOASAS Academic Repositories*, vol. 52, pp. 24–31, 2021.

[13] M. A. Trosheva et al., "Direct measurement of the genuine efficiency of thermogalvanic heat-to-electricity conversion in thermocells," *Chemical Science*, vol. 13, pp. 4984–4998, 2022.A. Kumar, A. Patel, S. Singh, A. Kandasami, and D. Kanjilal, "Apparatus for Seebeck coefficient measurement of wire, thin film, and bulk materials in the wide temperature range (80–650 K)," *Review of Scientific Instruments*, vol. 90, p. 104901, 2019.

[14] "Machine learning-driven multiobjective optimization of a MEMS in-situ thermoelectric Seebeck coefficient measurement structure," *Sensors and Actuators A: Physical*, 2025.

[15] F. Cougnon and D. Depla, "The Seebeck coefficient of sputter deposited metallic thin films: The role of process conditions," *Coatings*, vol. 9, no. 5, p. 299, 2019.

[16] H. Y. Lee, I. J. Yang, J.-H. Yoon, S.-H. Jin, S. Kim, and P. K. Song, "Thermoelectric properties of zinc-doped indium tin oxide thin films prepared using the magnetron co-sputtering method," *Coatings*, vol. 9, no. 12, p. 788, 2019.

Acknowledgements

We gratefully acknowledge the Institute of Physics at Nicolaus Copernicus University in Toruń for providing computational resources (PC), and the Institut des NanoSciences de Paris (INSP, Sorbonne Université/CNRS) for providing access to COMSOL Multiphysics® software, in support of this collaboration.